Modeling the High-Frequency Complex Modulus of Silicone Rubber Using Standing Lamb Waves and an Inverse Finite Element Method

Ulf G. Jonsson, Olof A. Lindahl, *Member, IEEE*, and Britt M. Andersson

Abstract—To gain an understanding of the high-frequency elastic properties of silicone rubber, a finite element model of a cylindrical piezoelectric element, in contact with a silicone rubber disk, was constructed. The frequency-dependent elastic modulus of the silicone rubber was modeled by a four-parameter fractional derivative viscoelastic model in the 100 to 250 kHz frequency range. The calculations were carried out in the range of the first radial resonance frequency of the sensor. At the resonance, the hyperelastic effect of the silicone rubber was modeled by a hyperelastic compensating function. The calculated response was matched to the measured response by using the transitional peaks in the impedance spectrum that originates from the switching of standing Lamb wave modes in the silicone rubber. To validate the results, the impedance responses of three 5-mm-thick silicone rubber disks, with different radial lengths, were measured. The calculated and measured transitional frequencies have been compared in detail. The comparison showed very good agreement, with average relative differences of 0.7%, 0.6%, and 0.7% for the silicone rubber samples with radial lengths of 38.0, 21.4, and 11.0 mm, respectively. The average complex elastic moduli of the samples were (0.97 + 0.009i) GPa at 100 kHz and (0.97 + 0.005i) GPa at 250 kHz.

I. Introduction

THE method of emitting ultrasonic waves into tissue and detecting the interaction of the waves with the tissue for medical purposes is now established as a standard method for detecting lesions in the tissue [1]. Because of the high cost of the equipment, screening for detection of various cancer forms is not a common procedure [2]. At polyclinics, there is a need for low cost, small, hand-held probes that can be used to monitor the existence of lesions in tissues, for example, prostate cancer [3].

A series of studies have been reported in which piezoelectric tactile sensors have been used to characterize soft tissue. These sensors can distinguish between normal and cancerous prostate tissue [4], [5]. Because the sensor is small and of the ready-to-use type, it could be a candidate for a new diagnostic instrument. The basic principle involves a piezoelectric sensor element, vibrating at resonance. The mass added to the sensor, resulting from the contact with soft tissue, results in a small change in the resonance frequency. The interpretation of this frequency shift is used to identify variations of the structural properties of the tissue. To improve this ability to detect structural variations, and to better understand the interaction between the vibrating piezoelectric element and soft tissue or tissue-like materials (phantoms), further investigation of the sensor and tissue/phantom combination is required.

When it comes to tissue-mimicking phantoms for ultrasound imaging, agarose- and gelatin-based phantoms have been used [6]. Specially designed for elastography imaging, gelatin-based phantoms with formaldehyde hardeners were investigated [7]. For evaluating the performance of a tactile piezoelectric sensor, a silicone rubber, has been used for phantoms [8]–[10]. This elastomer has also been used to model the elastic properties of the human skin [11]–[13].

The finite element method (FEM) is used today extensively to calculate the effects of structural vibrations. The creation of a FEM model of the tactile sensor-tissue system and fitting the model to measurements of the vibrational spectra will be an important step toward a deeper understanding of the interaction between the vibrating sensor and the soft tissue with which it is in contact. In the process of creating such a FEM model, as a first step, cylindrical piezoelectric elements have been characterized using a FEM model utilizing harmonic overtones [14].

In this work, the next step is taken, through FEM modeling of the viscoelastic properties of a tissue-like material that can be used as a phantom. A configuration with a single piezoelectric sensor, positioned in the center of a silicone rubber disk (SRD) emitting longitudinal waves into the disk, is used to model the viscoelastic properties of the SRD at the frequency range used by the tactile resonance sensor.

Human soft tissue and silicone rubbers have hyperelastic properties; i.e., they normally do not have a linear stress–strain relationship for large strains [15]. In shear wave elastography, linear models of the stress–strain relationship have been used because the displacements were

small and the strain rates were rapid (faster than 0.5/s) [7], [16], [17]. Modeling the frequency dependence of the elastic modulus in soft tissue is a key to gaining information about the existence of lesions.

Silicone rubbers are often used in applications in which its damping properties are utilized. Several models have been use to model the damping of viscoelastic materials. In the fractional derivative viscoelastic model (FDM), it is assumed that the stress is proportional to the strain derivative of fractional order [18], [19]. For finite element applications, the FDM has a great advantage of describing the relaxation properties with fewer parameters, covering the frequency spectrum, compared with conventional relaxation models such as the Maxwell model (a combination of sets of one spring in series with a dashpot) and the Voigt model (a combination of sets of one spring in parallel with a dashpot).

It has been shown that Lamb wave [20] dispersion ultrasound vibrometry can be used to quantify mechanical properties of soft tissues with plate-like geometry [21]. In this work, the configuration of the sensor and the disk, vibrating at the first radial resonance, enables symmetric Lamb waves to be established in the disk. Using an FDM of the viscoelastic properties of the SRD, together with the properties of standing Lamb waves, makes it possible to determine the frequency-dependent complex elastic modulus of the SRD. To get a better insight into the interaction between the sensor and the soft tissue using piezoelectric tactile sensors, a better understanding of the high-frequency elastic properties of silicon rubber is needed.

The purposes of this study were: 1) to develop a FEM model for a thick cylindrical piezoelectric element in contact with a viscoelastic silicone rubber disk. The vibrational modes in the silicone rubber disk can be detected by calculation of the frequency response of the impedance in the range of the first radial resonance of the piezoelectric element; 2) to model the complex elastic modulus of the silicone rubber disk using a fractional derivative model; 3) to validate the FEM model by a comparison of the calculated and measured impedance responses of silicone rubber disks with three different radial lengths.

II. METHOD

The piezoelectric sensor had a cylindrical shape with electrodes on its flat surfaces and was positioned in the center of the SRD, as shown in Fig. 1. The sensor was configured to excite radial waves into the SRD and to sense the response from the material by measuring the frequency response of the electric impedance of the sensor. The frequency range was chosen so that the impedance was measured at frequencies covering the first radial mode of the sensor.

Three 5-mm-thick SRD samples with radial lengths of 38.0, 21.4, and 11.0 mm were prepared; the samples were

named SG5x38, SG5x21, and SG5x11, respectively. The physical geometries and material specifications are given in Sections III-A and II-B, respectively. Throughout this paper, a primed parameter represents the real part and a double primed parameter represents the imaginary part.

A. The Finite Element PSM Equations

The finite element equations and boundary conditions presented in this section form an extension of the finite element partial equations solver model (PSM) [14]. The extension handles losses in the sensor and models the viscoelastic properties of the SRD. A finite element partial differential equations solver (FlexPDE, PDE Solutions Inc., Spokane Valley, WA) was used in the PSM.
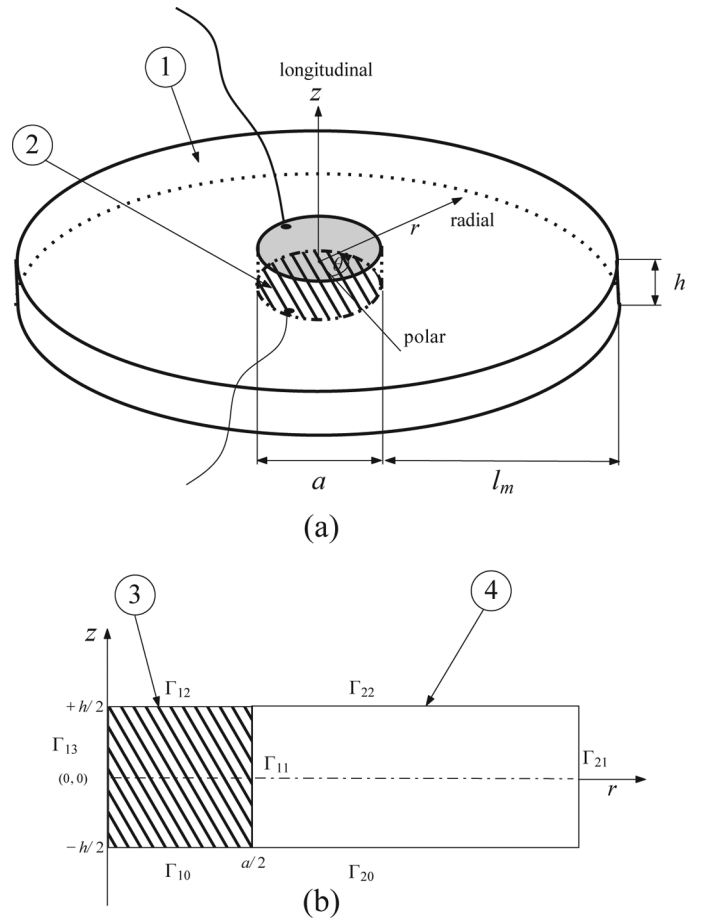

Fig. 1. (a) The measurement configuration oriented in a cylindrical coordinate system with radial, polar, and longitudinal axes (r, θ, z). (1) Silicone rubber, disk-shaped material of thickness h and radial length l_m; (2) the piezoelectric sensor, with electrodes on its flat surfaces and connecting electrical wires, positioned in the center of the disk, surrounded by the silicone rubber being measured. (b) Definition of the finite element problem areas: vertical half-plane cut through the sensor and the silicone rubber disk in the plane of the z-axis. (3) The problem area (hatched) of the sensor with boundaries Γ_{10}, Γ_{11}, Γ_{12}, and Γ_{13}; (4) the problem area representing the silicone rubber disk with boundaries Γ_{20}, Γ_{21}, Γ_{22}, and Γ_{11}.

1) The Piezoelectric Sensor Equations: The PSM was configured for a 2-D axisymmetric piezoelectric disk, acting as the sensor, in a cylindrical coordinate system (r, z), as shown in Fig. 1(a). The disk had a diameter-to-thickness ratio a/h. The system was assumed to be linear with small deviations from its equilibrium state. A vertical cross-section of the disk, shown in Fig. 1(b), was identified as the problem area for solving the partial differential equations that model the piezoelectric vibrations.

The mechanical system variables of the disk were the strain, S_q, and the stress, T_p. The 2-D cylindrical axisymmetric mechanical strain vector is given in abbreviated subscripts [22] by

$$S_q = \begin{bmatrix} u_{r,r}^* \\ u_r^*/r \\ u_{z,z}^* \\ 0 \\ 0 \\ u_{z,r}^* + u_{r,z}^* \end{bmatrix}, \quad (1)$$

where $u_r^* = u_r' + iu_r''$ and $u_z^* = u_z' + iu_z''$ are the displacement vectors, $u_{i,k}^* = \partial u_i^*/\partial x_k$, and $i^2 = -1$. (A comma followed by an index denotes partial differentiation with respect to a spatial coordinate.) The electric flux density, D_k, and the quasistatic electric field, $\mathcal{E}_i$, are the electric system variables. The elastic stiffness, piezoelectric, and inverted dielectric permittivity constants, listed in the Appendix, are denoted c_{pq}^D, h_{iq}, and β_{ik}^S, respectively. In this paper, the subscripts i, j, k, and l take the values 1, 2, or 3, and the subscripts p and q take the values 1, 2, 3, 4, 5, or 6 [23].

The piezoelectric constitutive equations with S_q and D_k as independent variables can be expressed as [23], [24]

$$T_p = c_{pq}^D S_q - \tilde{h}_{kp} D_k, \quad (2a)$$

$$\mathcal{E}_i = -h_{iq} S_q + \beta_{ik}^S D_k, \quad (2b)$$

with supporting equations

$$\text{div} D_k = 0, \quad (3a)$$

$$\mathcal{E}_i = -\varphi_{,i}^*, \quad (3b)$$

$$\text{div} T_p = -\omega^2 \rho u_i, \quad (3c)$$

where div is the cylindrical divergence operator [22], ρ is the density of the sensor, and $\varphi^* = \varphi' + i\varphi''$ is the electric potential. Eq. 3(c) represents the equation of motion, where we assume harmonic oscillations of type $e^{i\omega t}$ with the angular frequency $\omega = 2\pi f$, where f is the frequency.

A full treatment of the losses in the sensor requires implementation of loss factors in the viscoelastic, piezoelectric, and dielectric matrices. Because the frequency range of the sensor was limited to the first radial resonance mode, the loss factors were implemented as a subset in the viscoelastic matrix [25]. The loss in the sensor mod-

el was implemented as a viscoelastic loss tangent factor, η_{pq}, so that $c_{pq}^* = c_{pq}'(1 + i\eta_{pq})$, where $\eta_{pq} = c_{pq}''/c_{pq}'$.

Because of the axis-symmetry of the model, the derivatives of the displacement vector components with respect to θ can be ignored. Eq. 2(a) yields the real and imaginary components of the stress in cylindrical format:

$$T_{rr}' = c_{11}^D u_{r,r}' + c_{12}^D u_r'/r + c_{13}^D u_{z,z}' - \eta_{11} c_{11} u_{r,r}'' - \eta_{12} c_{12} u_r''/r$$
$$- \eta_{13} c_{13} u_{z,z}'' - \frac{e_{31}}{\varepsilon_{33}^S} D_z', \quad (4a)$$

$$T_{rr}'' = c_{11}^D u_{r,r}'' + c_{12}^D u_r''/r + c_{13}^D u_{z,z}'' + \eta_{11} c_{11} u_{r,r}' + \eta_{12} c_{12} u_r'/r$$
$$+ \eta_{13} c_{13} u_{z,z}' - \frac{e_{31}}{\varepsilon_{33}^S} D_z'', \quad (4b)$$

$$T_{\theta\theta}' = c_{11}^D u_r'/r + c_{12}^D u_{r,r}' + c_{13}^D u_{z,z}' - \eta_{11} c_{11} u_r''/r - \eta_{12} c_{12} u_{r,r}''$$
$$- \eta_{13} c_{13} u_{z,z}'' - \frac{e_{31}}{\varepsilon_{33}^S} D_z', \quad (4c)$$

$$T_{\theta\theta}'' = c_{11}^D u_r''/r + c_{12}^D u_{r,r}'' + c_{13}^D u_{z,z}'' + \eta_{11} c_{11} u_r'/r + \eta_{12} c_{12} u_{r,r}'$$
$$+ \eta_{13} c_{13} u_{z,z}' - \frac{e_{31}}{\varepsilon_{33}^S} D_z'', \quad (4d)$$

$$T_{zz}' = c_{13}^D u_r'/r + c_{13}^D u_{r,r}' + c_{33}^D u_{z,z}' - \eta_{13} c_{13} u_r''/r - \eta_{13} c_{13} u_{r,r}''$$
$$- \eta_{33} c_{33} u_{z,z}'' - \frac{e_{33}}{\varepsilon_{33}^S} D_z', \quad (4e)$$

$$T_{zz}'' = c_{13}^D u_r''/r + c_{13}^D u_{r,r}'' + c_{33}^D u_{z,z}'' + \eta_{13} c_{13} u_r'/r + \eta_{13} c_{13} u_{r,r}'$$
$$+ \eta_{33} c_{33} u_{z,z}' - \frac{e_{33}}{\varepsilon_{33}^S} D_z'', \quad (4f)$$

$$T_{rz}' = c_{44}^D(u_{z,r}' + u_{r,z}') - \eta_{44} c_{44}(u_{z,r}'' + u_{r,z}'') - \frac{e_{15}}{\varepsilon_{11}^S} D_r', \quad (4g)$$

$$T_{rz}'' = c_{44}^D(u_{z,r}'' + u_{r,z}'') + \eta_{44} c_{44}(u_{z,r}' + u_{r,z}') - \frac{e_{15}}{\varepsilon_{11}^S} D_r'', \quad (4h)$$

where $T_{rr}^* = T_{rr}' + iT_{rr}''$, $T_{\theta\theta}^* = T_{\theta\theta}' + iT_{\theta\theta}''$, $T_{zz}^* = T_{zz}' + iT_{zz}''$, $T_{rz}^* = T_{rz}' + iT_{rz}''$, and $T_{r\theta}^* = T_{\theta z}^* = 0$. Eq. 3(c) relates the divergence of the stress to the motion of the vibrating body. Application of the divergence operator to the stress yields the equations that describe the periodic elastic vibrations of the piezoelectric disk:

$$T_{rr,r}^* + T_{rz,z}^* + \frac{1}{r}(T_{rr}^* - T_{\theta\theta}^*) + \omega^2 \rho u_r^* = 0,$$
$$T_{zz,z}^* + \frac{T_{rz}^*}{r} + T_{rz,r}^* + \omega^2 \rho u_z^* = 0. \quad (5)$$

The second constitutional equation (2b), gives the components of the electric field:

$$\overline{c}_{pq} = \frac{E}{(1+\nu)(1-2\nu)}\begin{bmatrix} 1-\nu & \nu & \nu & 0 & 0 & 0 \\ \nu & 1-\nu & \nu & 0 & 0 & 0 \\ \nu & \nu & 1-\nu & 0 & 0 & 0 \\ 0 & 0 & 0 & (1-2\nu)/2 & 0 & 0 \\ 0 & 0 & 0 & 0 & (1-2\nu)/2 & 0 \\ 0 & 0 & 0 & 0 & 0 & (1-2\nu)/2 \end{bmatrix}. \tag{12}$$

$$\mathcal{E}_r^* = \frac{1}{\varepsilon_{11}^S}(D_r^* - e_{15}(u_{z,r}^* + u_{r,z}^*)), \tag{6}$$

$$\mathcal{E}_z^* = \frac{1}{\varepsilon_{33}^S}\left(D_z^* - e_{33}u_{z,z}^* - e_{31}\left(u_{r,r}^* + \frac{u_r^*}{r}\right)\right).$$

Substitution of (3b) into (6) gives the electric flux density components:

$$D_r^* = e_{15}(u_{z,r}^* + u_{r,z}^*),$$
$$D_z^* = e_{31}\left(u_{r,r}^* + \frac{u_r^*}{r}\right) + e_{33}u_{z,z}^* - \varepsilon_{33}^S\varphi_{,z}^*. \tag{7}$$

Application of (3a), the divergence of the electric flux density, yields

$$D_{r,r}^* + \frac{D_r^*}{r} + D_{z,z}^* = 0. \tag{8}$$

Eqs. (4), (5), and (8) make up the system of partial differential equations solved by the partial differential equation solver of the PSM to calculate the displacements in the sensor.

2) The Equations of Stress for the SRD (Linear Approximation): The silicone rubber was regarded as a homogeneous elastic material. Silicone rubbers are hyperelastic, which means that they have a nonlinear stress–strain relationship for large deformations. Because the vibrations that propagate in the silicone rubber from the piezoelectric element have very low displacement amplitudes, in this paper, the silicone rubber model was approximated to have a linear stress–strain relationship.

For an isotropic material, Hooke's law,

$$T_{ij} = \lambda S_{kk}\delta_{ij} + 2\mu S_{ij}, \tag{9}$$

where λ and μ are the Lamé's constants and δ_{ij} is the Kronecker delta, relates the stress to the strain of the material. The stiffness tensor

$$c_{ijkl} = \lambda\delta_{ij}\delta_{kl} + \mu(\delta_{ik}\delta_{jl} + \delta_{il}\delta_{jk}) \tag{10}$$

was calculated. Using the symmetric properties of the tensor, c_{ijkl} was abbreviated to c_{pq} [22].

The expression for c_{pq} together with the equations [20]

$$\lambda = \frac{E\nu}{(1+\nu)(1-2\nu)}, \quad \mu = \frac{E}{2(1+\nu)}, \tag{11}$$

was used to express the silicone rubber stiffness matrix $\overline{c}_{pq}$, in terms of the elastic modulus, E, and the Poisson's ratio, ν, as shown in (12), see above.

The viscoelastic properties of the silicone rubber were modeled using a fractional derivative model (see Section II-A-5) with a complex frequency-dependent elastic modulus $E^*(\omega)$. Hence, the coefficients of the stiffness matrix become complex $\overline{c}_{pq}^* = \overline{c}_{pq}' + i\overline{c}_{pq}''$. Because of the axis-symmetry of the model, the PSM equations of stress for the cylindrical axisymmetric SRD are

$$T_{rr}' = \overline{c}_{11}'u_{r,r}' - \overline{c}_{11}''u_{r,r}'' + (\overline{c}_{12}'u_r' - \overline{c}_{12}''u_r'')/r + \overline{c}_{12}'u_{z,z}' - \overline{c}_{12}''u_{z,z}'', \tag{13a}$$

$$T_{rr}'' = \overline{c}_{11}''u_{r,r}' + \overline{c}_{11}'u_{r,r}'' + (\overline{c}_{12}''u_r' + \overline{c}_{12}'u_r'')/r + \overline{c}_{12}''u_{z,z}' + \overline{c}_{12}'u_{z,z}'', \tag{13b}$$

$$T_{\theta\theta}' = \overline{c}_{12}'u_{r,r}' - \overline{c}_{12}''u_{r,r}'' + (\overline{c}_{11}'u_r' - \overline{c}_{11}''u_r'')/r + \overline{c}_{12}'u_{z,z}' - \overline{c}_{12}''u_{z,z}'', \tag{13c}$$

$$T_{\theta\theta}'' = \overline{c}_{12}''u_{r,r}' + \overline{c}_{12}'u_{r,r}'' + (\overline{c}_{11}''u_r' + \overline{c}_{11}'u_r'')/r + \overline{c}_{12}''u_{z,z}' + \overline{c}_{12}'u_{z,z}'', \tag{13d}$$

$$T_{zz}' = \overline{c}_{12}'u_{r,r}' - \overline{c}_{12}''u_{r,r}'' + (\overline{c}_{12}'u_r' - \overline{c}_{12}''u_r'')/r + \overline{c}_{11}'u_{z,z}' - \overline{c}_{11}''u_{z,z}'', \tag{13e}$$

$$T_{zz}'' = \overline{c}_{12}''u_{r,r}' + \overline{c}_{12}'u_{r,r}'' + (\overline{c}_{12}''u_r' + \overline{c}_{12}'u_r'')/r + \overline{c}_{11}''u_{z,z}' + \overline{c}_{11}'u_{z,z}'', \tag{13f}$$

$$T_{rz}' = \overline{c}_{44}'(u_{z,r}' + u_{r,z}') - \overline{c}_{44}''(u_{z,r}'' + u_{r,z}''), \tag{13g}$$

$$T_{rz}'' = \overline{c}_{44}''(u_{z,r}' + u_{r,z}') + \overline{c}_{44}'(u_{z,r}'' + u_{r,z}''). \tag{13h}$$

Eqs. (5) and (13) make up the system of partial differential equations solved by the partial differential equation solver of the PSM to calculate the displacements in the SRD.

3) Poisson's Ratio and the 2-D FEM: Biological tissues and rubber-like materials are incompressible, i.e., they have a Poisson's ratio $\nu \approx 0.5$. For an isotropic elastic material, ν is related to λ and μ by

$$\lambda = \frac{2\mu\nu}{1-2\nu}, \tag{14}$$

TABLE I. PSM BOUNDARY VALUE CONDITIONS
OF THE SENSOR PROBLEM AREA.

Boundary	Type of condition		
Γ_{10}	load(u_r^*)	load(u_z^*)	value(φ^*)
Γ_{11}	load(u_r^*)	load(u_z^*)	load(φ^*)
Γ_{12}	load(u_r^*)	load(u_z^*)	value(φ^*)
Γ_{13}	value(u_r^*)	load(u_z^*)	load(φ^*)

The displacements u_r^*, u_z^* and the electric potential φ^* are all complex parameters. For all boundary value conditions load(), value(), the real and imaginary parts are set to zero except for boundary Γ_{12}, where the real part of value(φ) is set to equal to the excitation voltage. At the origin $(0,0)$, a single point value (u_r^*, u_z^*) was set equal to zero to allow only axisymmetric extensional mode vibrations.

which is not defined for $\nu = 0.5$. Hence, when performing finite element calculations using a linear isotropic elasticity model, numerical instabilities arise when letting $\nu \to 0.5$. It has been shown, under certain conditions, that for a 2-D representation of the geometry, the Poisson's ratio can be expressed as $\nu' = \nu/(1 + \nu)$ by regarding a unit cube of incompressible elastic material [26].

The expression for ν' was derived by regarding a unit cube[1] of incompressible elastic material with axial, x_1, lateral, x_2, and elevational, x_3, orthogonal axes. The axial surfaces at $x_1 = 1$ and $x_1 = 0$ are allowed to expand in the lateral and elevational directions. The lateral surfaces, orthogonal to the lateral axis, and the elevational surfaces, orthogonal to the elevational axis, of the unit cube are free to move. The axial surface at $x_1 = 1$ is subjected to a small axial compression (along x_1). The displacements (u_1, u_2) are measured in a 2-D plane at $x_3 = 0$. It can be shown [26] that the displacements (u_1, u_2) are the same as the displacements (u_1', u_2') of an incompressible plane strain model used to calculate the displacements in a 2-D plane at $x_3 = 0$ with $\nu' = \nu/(1 + \nu)$. In the plane strain model, the elevational surfaces are clamped or the material is regarded infinite.

The preceding arguments can be extended to the cylindrical element depicted in Fig. 2. A surface of the element is denoted by the axis to which the surface is orthogonal. The element is considered to belong to an axisymmetric cylindrical body such as the SRD in Fig. 1. The situation is analogous to the unit cube case: let a small compression act in the radial direction with the radial surfaces free to expand in the longitudinal and polar directions. Measurements of the displacements (u_r, u_z) in the problem plane indicated in Fig. 2 correspond to measurements of the displacements in the unit cube plane $(x_3 = 0)$ [26]. The longitudinal surfaces are allowed to move freely. In the polar direction, which corresponds to the elevational direction in the unit cube case, because of the axisymmetric assumption, the polar displacements, u_θ, are all zero. Hence, the polar surfaces could be regarded as clamped. Thus, when we used the 2-D cylindrical finite element model to
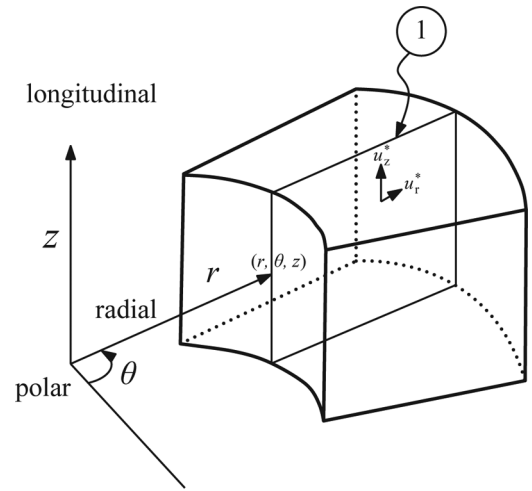
[1]The paragraph concerning the unit cube case is reproduced from Fehrenbach [26] for clarity.

Fig. 2. Cylindrical element with radial, polar, and longitudinal axes (r, θ, z); (1) finite element problem plane. u_r^*, u_z^* are complex displacements in the problem plane.

calculate the displacements for the axisymmetric SRD, we used an axisymmetric cylindrical model with the Poisson's ratio set to ν'.

Using this conversion of the Poisson's ratio and comparing the calculated results of a 3-D model to a 2-D plane strain model results in relative displacement differences in the radial and vertical directions of <1% and <10%, respectively [26]. Because the waves emitted in to the SRD are radial, the deviation in vertical displacements has minimal impact. The 2-D finite element model, when compared with a 3-D model, cannot replicate any potential vibrational modes in the θ-direction (Fig. 2).

4) The Boundary Value Conditions of the Sensor and SRD Problem Areas: The boundaries of the sensor problem area are shown in Fig. 1(b). The boundaries Γ_{12} and Γ_{10} are defined in the planes of the electrodes in the figure. Boundaries Γ_{11} and Γ_{13} are parallel to the z-axis at $r = a$ and $r = 0$, respectively. The electrodes were connected to an alternating voltage source, $Ve^{i\omega t}$, generating a vertical electric field. The boundary conditions are listed in Table I. The value function specifies the value that a dependent variable must take at a boundary of the domain. The load function specifies the value that the normal component of the gradient of the dependent variable should have at the boundary of the domain. At the origin $(0,0)$, a single point value(u_r^*, u_z^*) was set equal to zero to allow only axisymmetric extensional mode vibrations. The electric potential φ^* was set to zero at Γ_{10} and to the value of the exciting voltage at boundary Γ_{12}.

The boundary conditions for the SRD problem area are listed in Table II. The sensor and the SRD are connected by boundary Γ_{11}. The boundary condition at Γ_{11} was set so that the normal component of the stress was continuous across the boundary. To enable standing Lamb waves in the SRD, a mixed boundary condition [27] was set for boundaries Γ_{20} and Γ_{22}, where the radial displacement, u_r^*,

TABLE II. PSM BOUNDARY VALUE CONDITIONS OF THE SILICONE RUBBER DISK PROBLEM AREA.

Boundary	Type of condition	
Γ_{20}	value(u_r^*)	load(u_z^*)
Γ_{21}	load(u_r^*)	load(u_z^*)
Γ_{22}	value(u_r^*)	load(u_z^*)
Γ_{11}	value(u_r^*)	load(u_z^*)

The displacements u_r^*, u_z^* are complex parameters. For all boundary value conditions load(), value(), the real and imaginary parts are set to zero except for boundaries Γ_{20} and Γ_{22}, where the **value**(u_r^*) is set to zero to enable Lamb standing waves.

was set to zero. The curved surface of the SRD was set to move freely.

5) The Fractional Derivative Viscoelastic Model (FDM): Rubber-like materials exhibit a frequency-dependent viscoelastic property that can be modeled by a complex elastic modulus $E^*(\omega)$

$$E^*(\omega) = E'(\omega) + iE''(\omega), \tag{15}$$

where $E'(\omega)$ is the real part or the storage modulus and $E''(\omega)$ is the imaginary part or the loss modulus. Analogous to dielectric relaxation, the loss tangent, $\tan\delta(\omega) = E''(\omega)/E'(\omega)$ indicates the damping of propagating acoustic waves in the material.

In the FDM, it is assumed that the stress is proportional to the strain derivative of fractional order [18]. For finite element applications, the FDM has a great advantage of describing the relaxation properties with few parameters covering the frequency spectrum.

The four-parameter FDM [28],

$$E^*(\omega) = \frac{E_0 + E_\infty(i\omega\tau_c)^\alpha}{1 + (i\omega\tau_c)^\alpha}, \tag{16}$$

where E_∞ and E_0 are the moduli at the high- and low-frequency limits, respectively; τ_c is a characteristic time constant; and the frequency $\omega_c = 1/\tau_c$ is the maximum frequency of the loss modulus peak. The parameter α controls the slope of the symmetric loss function ($0 < \alpha < 1$) [19].

The modulus $E^*(\omega)$ can be expressed in its real and imaginary parts:

$$E'(\omega) = E_0 \left\{ 1 + \frac{k[\cos(\pi\alpha/2)(\omega\tau_c)^\alpha + (\omega\tau_c)^{2\alpha}]}{1 + 2\cos(\pi\alpha/2)(\omega\tau_c)^\alpha + (\omega\tau_c)^{2\alpha}} \right\}, \tag{17}$$

$$E''(\omega) = E_0 \frac{k\sin(\pi\alpha/2)(\omega\tau_c)^\alpha}{1 + 2\cos(\pi\alpha/2)(\omega\tau_c)^\alpha + (\omega\tau_c)^{2\alpha}}, \tag{18}$$

and the loss tangent

$$\tan\delta(\omega) = \frac{k\sin(\pi\alpha/2)(\omega\tau_c)^\alpha}{1 + k[\cos(\pi\alpha/2)(\omega\tau_c)^\alpha + (\omega\tau_c)^{2\alpha}]}, \tag{19}$$
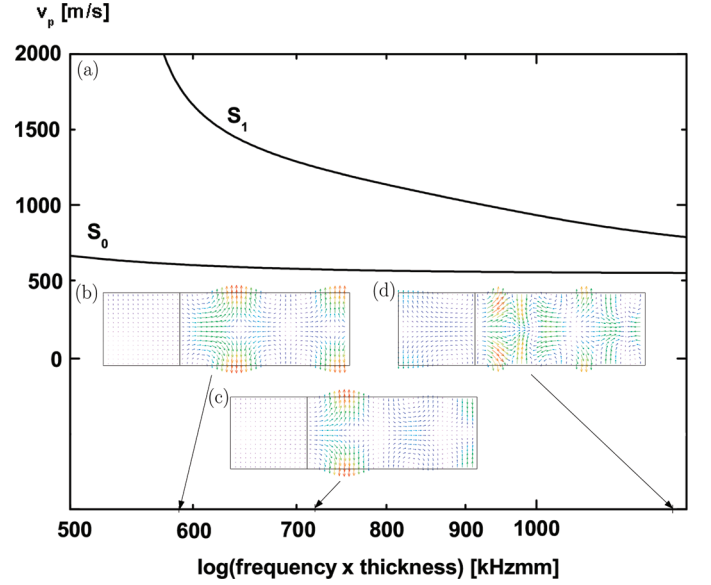

Fig. 3. The first two symmetric dispersion curves, S_0 and S_1, calculated with Waveform Revealer, for a 5-mm-thick silicone rubber plate, with ρ = 970 kg/m³, E = 1.0 GPa, and ν = 0.499. (a) The wave velocity v_p is plotted versus the frequency–thickness in the actual range. Mode shape plots of the displacements at frequency–thicknesses (b) 582 kHz·mm, (c) 721 kHz·mm, and (d) 1227 kHz·mm are shown in the insets. The shape plots are Lamb wave transitions of the sample SG5x11.

where $k = E_\infty/E_0 \gg 1$ [19].

6) Standing Lamb Waves in the SRD: Because of the radial excitation of the vibrations into the SRD, the favored Lamb wave modes in the SRD in the actual frequency–thickness range are the symmetric modes S_0 and S_1. A dispersion plot calculated using the computer program Wave Form Revealer 3.0 (Laboratory for Active Materials and Smart Structures, University of South Carolina, Columbia, SC) for a 5-mm plate of the silicone rubber is shown in Fig. 3(a). In the dispersion plot, the S_0 mode is the only mode that exists in the low-frequency regime. The S_1 mode is nonexistent below its nascent frequency–thickness of approximately 600 kHz·mm. The three shape plots in Figs. 3(b)–3(d) show the displacements as a result of the superposition of the S_0 and S_1 modes. The S_0 mode dominates at the low-frequency part of the calculated frequency range, whereas the S_1 mode dominates at the high-frequency part of the frequency range. In the intermediate frequency range, both modes are present and interfere, which can be seen as a modulation of the envelope in the shape plots.

B. Finding the PSM Model Parameters of the Combined System of Sensor and SRD

In the following two sections, the parameters E^{ini}, α, and the hyperelastic compensating function $\Phi(\omega)$ are referenced. Detailed descriptions concerning each parameter can be found in Section II-B-2 for E^{ini}, Section II-B-3 for α, and Section II-B-4 for $\Phi(\omega)$.

The density, thickness, and diameter of the piezoelectric sensor, and the density and radial length of the SRD were set to fixed values and were not part of the fitting procedure. The piezoelectric sensor and the SRD were modeled by two separate sets of constitutive equations describing the piezoelectric sensor itself and the SRD connected at a boundary with appropriate boundary conditions as described in Sections II-A-1, II-A-2, and II-A-4.

The following parameters described the vibrational characteristics of the sensor: the elastic parameters c_{11}, c_{12}, c_{13}, c_{33}, and c_{44}; the piezoelectric parameters e_{31}, e_{15}, and e_{33}; the dielectric parameters ε_{11} and ε_{33}; and the loss tangent, η. Because the sensor was identical to a piezoelectric element (PZT-5A1, Morgan Electro Ceramics, Thornhill, Southampton, England) that was modeled in an earlier work, the PD02 model [14], the parameters were identical to the effective PD02 model parameters with the addition of the loss tangent parameter.

The silicone rubber SG612 (SilGel 612, Wacker Chemie, München, Germany) was used in the SRDs. The SG612 was regarded as nearly incompressible. The Poisson's ratio ν was set to the fixed value 0.49. Details on the silicone rubber are in Section III-A.

The complex elastic modulus $E^*(\omega)$ of the silicone rubber was implemented in the stiffness matrix $\overline{c}^*_{pq}$. $E^*(\omega)$ was modeled by the FDM, (16)–(19). For frequencies near the radial resonance, the hyperelastic compensating function $\Phi(\omega)$, (21), modifies the elastic modulus.

1) The PSM Parameter Fitting Procedure: In the procedure of fitting parameters, the sensitivity of the parameters was determined by calculating the sensitivity matrix ξ_{nm}. The elements of the matrix are the ratios of the relative variation of target frequency–thicknesses to the relative variation in parameter values [14]. The parameters were tuned using the feedback algorithm for the determination of grouped parameters [14], here called the parameter tuning procedure (PTP).

As shown in the sensitivity matrix for the SG5x11 model, Table III, the elements for the parameters α and τ_c demonstrate low sensitivity values which made fitting using the PTP difficult. The effects of the time constant τ_c and the fractional exponent α are related. A variation of τ_c moves the peak frequency of E'' and a variation of α has the effect of altering the slope of $\log(E'')$ when plotted versus $\log(\text{frequency})$. This means that the effect of a variation in τ_c can be neutralized by a variation of α. Therefore, it was decided to determine the parameter α by a procedure external to the method of using Lamb wave transition frequencies. This procedure is described in Section II-B-3.

The procedure to fit the PSM parameters was divided into three consecutive stages:

1) The baseline tuning stage: The SRD, when connected to the piezoelectric sensor, will superimpose resonance peaks to the baseline impedance response in
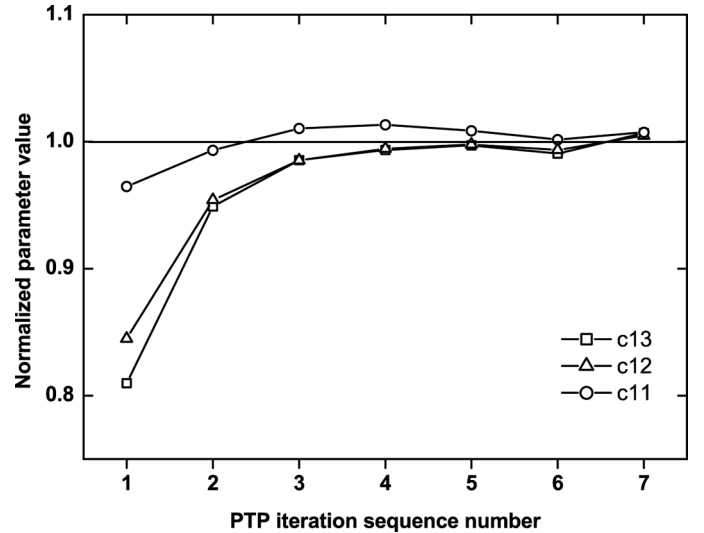

Fig. 4. Convergence of the elastic parameters c_{11}, c_{12}, and c_{13} using the parameter tuning procedure PTP.

the first radial resonance mode interval. To match the baseline of the PSM model to the measured baseline, the elastic parameters c_{11}, c_{12}, and c_{13} of the sensor were used. They are dominant in the low-frequency tuning stage sensitivity matrix [14] for the R_1 and R_1^a radial resonances. The parameters were tuned using the PTP. The convergence of the parameters c_{11}, c_{12}, and c_{13} using the PTP is shown in Fig. 4.

2) The viscoelastic tuning stage: The viscoelastic properties of the SRD were modeled by the FDM. The initial elastic modulus, E^{ini}, was used together with the low-frequency limit value of the elastic modulus, E_0, so that the initial k value for the fitting procedure was $k = E^{\text{ini}}/E_0$.

Before fitting the FDM parameters, the sensitivity matrix ξ_{nm} was determined. As target frequencies, the first three transition frequencies were chosen of the measured SRD samples. The reason for this is that in each frequency response for each sample, the most suitable frequencies are the ones at lower frequencies, away from the radial resonance frequency, with minimal impact from the hyperelastic effect. The SG5x11 sample had only three Lamb wave transitions below the radial resonance frequency, so it was decided to use the same number for all samples. The time constant τ_c was determined by successive calculations of the impedance response of the

TABLE III. THE VISCOELASTIC TUNING STAGE PARAMETER SENSITIVITY MATRIX ξ_{NM} FOR SAMPLE SG5x11.

f^h [kHz·mm]	k	α	τ_c
497.0	$\xi_{11} = 0.442$	$\xi_{12} = 0.014$	$\xi_{13} = 0.002$
582.0	$\xi_{21} = 0.505$	$\xi_{22} = 0.013$	$\xi_{23} = 0.002$
669.5	$\xi_{31} = 0.500$	$\xi_{32} = 0.010$	$\xi_{33} = 0.001$

The frequency–thicknesses, f^h, are not corrected for the hyperelastic effect.

TABLE IV. THE HYPERELASTIC COMPENSATING TUNING STAGE
PARAMETER SENSITIVITY MATRIX ξ_{NM} FOR SAMPLE SG5x38.

| f_n^{h} [kHz·mm]	κ	ω_0	$d\omega$
685.6	$\xi_{11} = 0.284$	$\xi_{12} = -0.142$	$\xi_{13} = 0.014$
774.4	$\xi_{21} = 0.452$	$\xi_{22} = -0.195$	$\xi_{23} = -0.002$
863.8	$\xi_{31} = 0.337$	$\xi_{32} = -0.045$	$\xi_{33} = -0.011$

Fig. 5. The displacements of the SG5x21 silicone rubber disk model showing the standing Lamb wave pattern. The square to the left represents the sensor problem area ($(a/2) \times h$). The rectangle to the right represents the problem area ($l_m \times h$) of the silicone rubber disk.

SG5x38 model. By adjusting the time constant τ_{c}, the amplitude of the first three transitions were set equal to the measured transitions within ± 0.5 dB. The value found through the fitting process for τ_{c} was also used for the SG5x21 and SG5x11 models. The parameter k was determined using the PTP and the viscoelastic tuning stage sensitivity matrix.

3) The hyperelastic compensating tuning stage: For frequencies near the radial resonance, the function $\Phi(\omega)$ compensates the decrease in the elastic modulus caused by the increase in the displacement amplitudes. The parameters were determined using the PTP with the hyperelastic stage tuning parameter sensitivity matrix. In Table IV, the sensitivity matrix is listed for the SG5x38 SRD. The target frequency-thicknesses were f_4^{h}, f_6^{h}, and f_8^{h} for the SG5x38 model; f_1^{h}, f_3^{h}, and f_6^{h} for the SG5x21 model; and f_1^{h}, f_2^{h}, and f_3^{h} for the SG5x11 model. Values for the target frequency-thicknesses are listen in Section IV-A.

The effective thickness, h^{e}, of a SRD was found by shifting the calculated frequency-thickness response, i.e., multiplying the frequency with an increasing or decreasing thickness until the relative difference, Δ_n, of the selected transition frequencies was minimized. The thickness leading to the minimum Δ_n was set as h^{e}.

The relative difference was defined as

$$\Delta_n = \sqrt{\frac{1}{n} \sum_{m=1}^{n} \left(\frac{f_m^{\mathrm{hc}} - f_m^{\mathrm{he}}}{f_m^{\mathrm{he}}} \right)^2}, \qquad (20)$$

where n equals the number of transitions, and f_m^{hc} is the mth calculated and f_m^{he} is the mth measured impedance response transition frequency-thickness. Δ_n was calculated for each change in the thickness. The frequency-thicknesses used are listed in Section IV-A for each sample.

2) Procedure to Find the Initial Elastic Modulus, E^{ini}: While establishing the initial value, E^{ini}, it was observed that when sweeping the modulus from low to high values—typically 0.1 to 2 GPa—the transitional peaks in the calculated impedance response did not generate one unique match to the measured impedance response. A procedure was implemented that would point out possible values of E^{ini}. The model of the SG5x21 SRD is used to explain the steps involved; the same arguments hold for the SG5x38 and the SG5x11 SRD models.
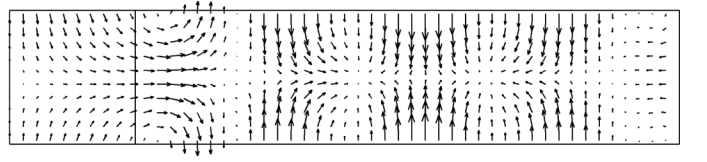
First, a characteristic standing Lamb wave mode was selected, as shown in Fig. 5 for the SG5x21 SRD. The mode was chosen at the low end of the frequency interval so that the influence from the peak in the radial resonance was minimal and the mode was stable between mode transitions. The selected standing Lamb wave mode has two associated frequencies f_{i} and f_{o}, where f_{i} is the transition frequency into the mode and f_{o} is the transition out of the mode, and where $f_{\mathrm{i}} < f_{\mathrm{o}}$. Next, calculations of the impedance response of the SRD model were carried out in which the modulus was varied between 0.1 to 1.7 GPa. For each value of the modulus, the impedance response was plotted with the measured response versus the frequency-thickness product. The calculated impedance transition at f_{i} was matched to the measured transition by adjusting the effective thickness of the SRD model while preserving the number of transitions to the first radial resonance frequency. This was possible because the impedance response of the SRD is invariant when plotted versus the frequency-thickness product for different thicknesses. Finally, the effective thickness, h^{e}, was plotted versus the modulus. From the plot, possible values of E^{ini} were found for values of h^{e} equal to the real thickness of the SRD. The calculations were carried out for a 5.0-mm-thick SRD disk. For a disk with physical thickness below 5.0 mm, the plot was extrapolated to the physical value as shown in Fig. 6. If more than one value was found, the E^{ini} value that generated the response that best corresponded to the measured response was selected.

3) Finding an Initial Value for the FDM Parameter α: The parameter α and the static elastic modulus of three fluoroelastomers were determined by others [19]. The values were (α, E_0 [MPa]): $(0.65, 0.74)$; $(0.60, 1.44)$; and $(0.51, 2.08)$, respectively. The hardness of the silicone rubber SilGel 612 was measured by the manufacturer (private communication, Wacker-Kemi, Stockholm, Sweden, Nov 2011) for different ratios of the components A and B. For the ratio A/B = 1.6 which was used in this work, the hardness measured with scale Shore-000 was 82. Using the conversion procedure described in [29], this hardness value corresponds to a static elastic modulus of 0.70 MPa for the SRD, which is near the value that was found for the first fluroelastomer measured in [19]. Using the assumption that elastomers, at zero frequency, which have the same static elastic modulus will approximately have the same α value yields an initial estimation of $\alpha = 0.65$.
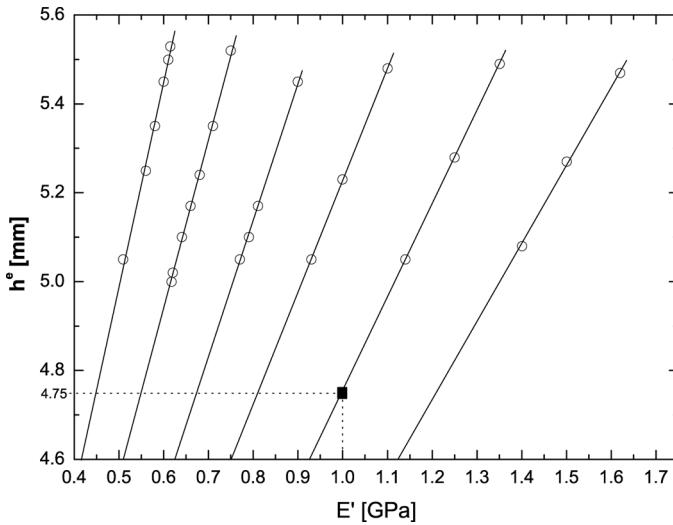
Fig. 6. The PSM-calculated effective thickness, h^e, determined using a 5-mm-thick SG5x21 model where two Lamb wave transitions are used in the determination, versus the elastic modulus E'. (Open circles) thickness and elastic modulus where the selected Lamb wave transition matches (Section II-B-2); (solid lines) extrapolated to values below 5.0 mm; (solid square) elastic modulus chosen as $E^{ini} = 1.0 \pm 0.05$ GPa for a 4.75-mm-thick silicone rubber disk.
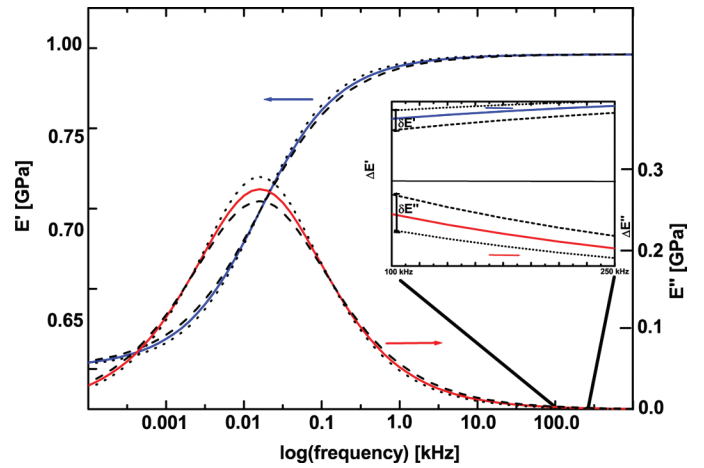

Fig. 7. The real part E' and the imaginary part E'' of the elastic modulus calculated using the fractional derivative model, FDM, plotted for the SG5x38 sample with parameters $k = 1.40 \times 10^3$, $\alpha = 0.65$, $\tau_c = 10$ ms. Plots: (blue line) E'; (red line) E''. (Dotted line) the parameter α is increased by 5.0%; (dashed line) the parameter α is decreased by 5.0%. Enlarged in the inset is the relative variation of $\Delta E'$ and $\Delta E''$ for the frequency range of the finite element calculations. $\delta E' = \pm 0.06\%$; $\delta E'' = \pm 23\%$. The relative variation of $\delta E''$ to the maximum value at the frequency 16 Hz is $\pm 24\%$.

To investigate the impact on the real and the imaginary part of $E^*(\omega)$, calculations using the FDM were carried out in which α was varied $\pm 5.0\%$. A plot of the result is shown in Fig. 7. The maximum relative variation of the real part, E' was $\pm 0.06\%$ in the frequency range of the calculations. The maximum relative variation of the imaginary part, E'' was $\pm 23\%$ in the frequency range of the calculations and $\pm 0.24\%$ relative the maximum value of E'' at the frequency 16 Hz.

4) The Hyperelastic Compensating Function $\Phi(\omega)$: Modeling the vibrational characteristics of the combined system of the sensor and the SRD at the first radial resonance means that the model must also be able to handle the range of displacement amplitudes when the system goes into resonance. As the frequency of vibration approaches the resonance frequency, the mechanical system becomes unstable and the displacement amplitude increases rapidly. The silicone rubber is a hyperelastic material, which means that the linear Hooke's model is not valid for large strains and is normally superseded by a nonlinear model for rubber-like materials [15]. The vibrating displacements of the silicone rubber, on the other hand, are very small but increase significantly when approaching the radial resonance. The increase in the amplitude of the displacements at resonance increased the nonlinearity of the system, which made fitting of the calculated and measured resonance responses impossible at the radial resonance.

The Payne effect [30] is a hyperelastic effect in which a decrease in the complex elastic modulus is a consequence of increasing periodic strain amplitudes. The situation for the SRD is similar, in that sense that there is a radical increase in the displacement amplitudes when approaching

the radial resonance frequency. It was assumed that the most probable explanation for the observed effect had its origin in the Payne effect. To compensate for the decrease in the elastic modulus, a Boltzmann function (sigmoidal) was introduced as a compensating function:

$$\Phi(\omega) = (1 - \kappa)/(1 + e^{((h^e(\omega - \omega_0))/2\pi)/d\omega}) + \kappa, \qquad (21)$$

where $\kappa = \lim_{\omega \to \infty} \Phi(\omega)$, h^e is the effective thickness of the SRD, ω_0 is the frequency at which $\Phi(\omega_0) = (\kappa + 1)/2$, and $d\omega$ controls the slope of the curve. The product of the compensating function and the elastic modulus, $E^*(\omega)\Phi(\omega)$, compensates the elastic modulus for the hyperelastic effect in the frequency range of the first radial resonance. A plot of compensated and uncompensated impedance responses for the SG5x21 sample can be found in Fig. 8.

5) Reference Measurement: To verify that $\Phi(\omega)$ was ultimately associated with the properties of the SRD, a reference measurement was carried out on a polyamide disk (Andramid PA6GPE, Andrén & Söner, Stockholm, Sweden). The PA6GPE disk was 5 mm thick, with a radial length of 20.6 mm. The measurement was carried out at room temperature, which was well below the glass transition temperature of the material. The piezoelectric sensor was placed in the center of the disk by carefully positioning it in a drilled hole with the same diameter as the sensor. To increase the acoustic coupling to the disk, ultrasound gel was used on the contact surface between the sensor and disk. The disk was suspended from a 0.1-mm fishing line glued to the outer periphery, which allowed all sides of the disk to move freely. The electric impedance was measured with a network analyzer (Agilent E5100A/B,
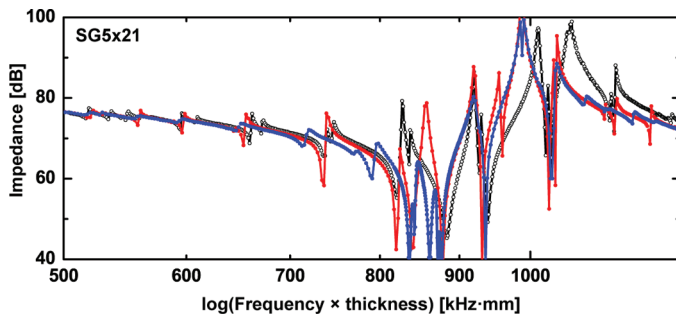
Fig. 8. Effect of the hyperelastic compensating function $\Phi(\omega)$. Compensated and uncompensated impedance responses for the SG5x21 sample. Plot: (filled red circles) compensated response, (filled blue circles) uncompensated response, (open circles) the measured response.

Agilent Technologies Inc., Santa Clara, CA) from 100 kHz to 250 kHz with a frequency step resolution of 0.25 kHz.

In Fig. 9, the calculated and measured impedance responses of the polyamide PA6GPE sample are plotted. The calculated response is without the hyperelastic compensating function $\Phi(\omega)$. The FDM parameters were $k = 3.15 \times 10^5$, $\alpha = 0.65$, and $\tau_c = 1000$ mS. The Poisson's ratio was set to $\nu = 0.39$ [31]. The elastic modulus of the sample in the measured frequency interval was determined to 3.2 GPa. The value of the elastic modulus provided by the manufacturer was 3.1 GPa.

III. Experimental Procedure

A. Preparation of the Silicone Rubber Disks

Three silicone rubber disks with different radial lengths were configured to confirm that the Lamb wave mode switching was consistent with the same finite element model for all lengths. The purpose was to study if the hyperelastic effect differed between samples. To measure the electric impedance response of the SRD samples, a measurement setup was configured with a cylindrical piezoelectric sensor placed in the center of the SRD as shown in Fig. 1.

The thickness of the piezoelectric sensor and the radial lengths of the SRDs were determined using a caliper (No.102–217, Mitutoyo Corp., Kawasaki, Japan). The thickness of the sensor was 5.04 ± 0.01 mm. The radial lengths of the silicone rubber disks, l_m, were 38.0 ± 0.05 mm for sample SG5x38, 21.4 ± 0.05 mm for sample SG5x21, and 11.0 ± 0.05 mm for sample SG5x11. The diameter-to-thickness ratio, a/h, of the piezoelectric sensor was 1.98 ± 0.01. The thickness of an SRD was determined when the mold was filled with the uncured silicone rubber mixture. Because of the adhesive effect of the fluid, the thickness of the disk was not constant along the radius, with a small increase in the thickness at the boundaries of the sensor and the mold. The average thicknesses of the SG5x38, SG5x21, and SG5x11 disks were determined with
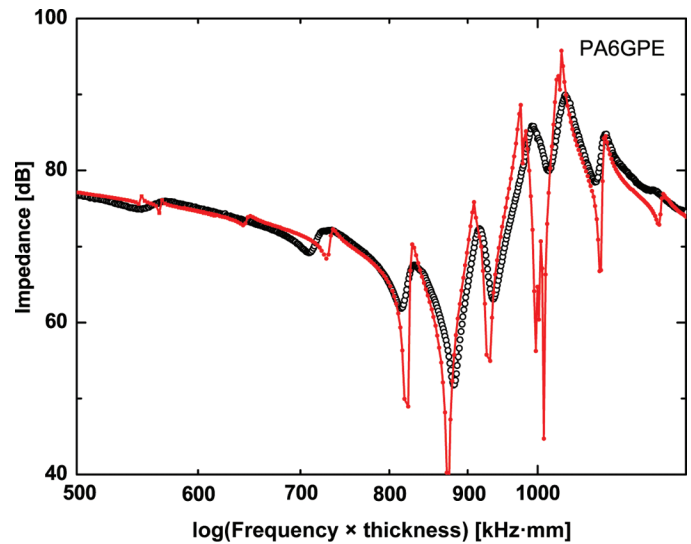

Fig. 9. The frequency response of the measured, and PSM calculated, impedance of the PZT-sensor in contact with a 5-mm-thick polyamide (PA6GPE) disk. The calculation was carried out with no hyperelastic compensating function. Plot: (open circles) measured response, (filled red circles) PSM calculated response.

the caliper to be 4.70 ± 0.05 mm, 4.75 ± 0.05 mm, and 5.15 ± 0.05 mm, respectively.

The SG612 is a two-component addition-curing silicone rubber that vulcanizes at room temperature. The samples were created by mixing 4 parts of component A and 2.5 parts of component B (A/B = 1.6). The mixture was stirred for 5 min and then poured into a mold, after which it was set to cure for 24 h. After curing, the mold was removed by carefully cutting the mold into small parts. The mold was constructed using a Petri dish made of polystyrene with the piezoelectric sensor mounted in the center of the dish.

B. Measuring the Electrical Impedance Response of the SRD

The electric impedance of the sensor was measured using the network analyzer. The analyzer was configured to measure the real and imaginary parts of the impedance as a function of frequency. The measurements were carried out at room temperature with air as surrounding medium. The impedance was measured in the frequency range of 100 to 250 kHz, where the piezoelectric sensor has its first radial resonance mode [14]. The impedance was measured with a 0.25 kHz frequency step resolution. The power input to the sensor was set to -60 dB·mW to minimize system nonlinearity. The flat surfaces of the piezoelectric sensor and all sides of the SRD not in contact with the sensor were allowed to move freely by suspending the disk from a 0.1-mm fishing line that was attached to the outer periphery of the disk.

The measured data were corrected for instrumental scaling factors and parasitic inductances [14]. After com-

TABLE V. RESULTS OF THE PSM AND FIXED VALUES OF THE BASELINE TUNING STAGE FOR THE PIEZOELECTRIC SENSOR IN THE 100 TO 250 kHz FREQUENCY RANGE, WITH ESTIMATED UNCERTAINTY Δu.

Parameter[1]	Fixed value[2]	PTP value[3]	Δu
c_{11} [10^{10} N/m^2]		13.2	±0.05
c_{12}		6.28	±0.02
c_{13}		7.75	±0.03
c_{33}	11.4		
c_{44}	2.16		
e_{31} [C/m^2]	−3.09		
e_{33}	15.3		
e_{15}	8.85		
$\varepsilon_{11}/\varepsilon_0$	916		
$\varepsilon_{33}/\varepsilon_0$	783		
η	0.002		
ρ_s [kg/m^3]	7750		

[1]$\varepsilon_0 = 8.854 \times 10^{12}$ F/m.
[2]Values acquired from external source [14].
[3]Values determined using the parameter tuning procedure PTP.

Fig. 10. The real part, $E'(\omega)$, to the left, and the imaginary part, $E''(\omega)$, to the right, of the elastic modulus versus frequency–thickness for the silicone rubber samples SG5x38, SG5X21, and SG5x11 calculated with the fractional derivative model parameters from Table VI.

pletion of the measuring sequences, the data were transferred to a desktop computer for post-processing.

IV. RESULTS

A. Results of the Parameter Fitting Sequence

The results of the fitting procedure are tabulated in Tables V and VI. The results of the procedure to establish the initial elastic modulus value, E^{ini}, are plotted in Fig. 6. From the plot, the value $E^{\text{ini}} = 1.0 \pm 0.05$ GPa was found for the effective thickness equal to the measured
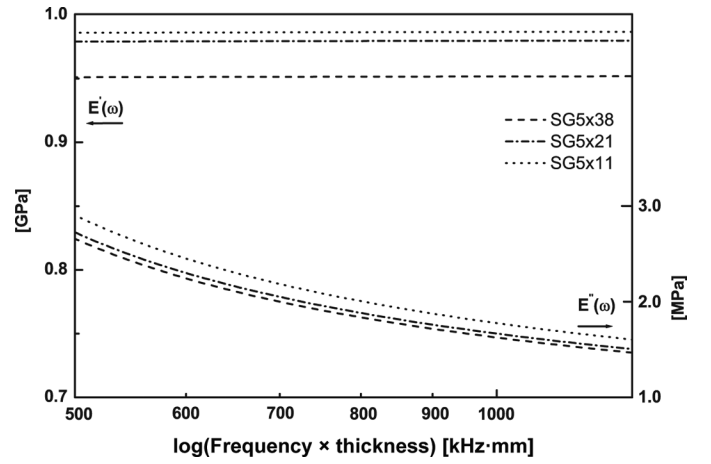
thickness $h^{\text{e}} = 4.75$ mm for the SG5x21 sample. The same E^{ini} value was also used for the SG5x38 and SG5x11 samples. In Fig. 10, the real and imaginary parts of the FDM-modeled complex elastic modulus $E^*(\omega)$, with parameters from Table VI are plotted in the frequency range 100 to 250 kHz for the SG5x38, SG5x21, and SG5x11 samples. The average value of the complex modulus for all samples were $(0.97 + 0.009\text{i})$ GPa at 100 kHz and $(0.97 + 0.005\text{i})$ GPa at 250 kHz.

In Fig. 11, the hyperelastic compensating function $\Phi(\omega)$ for each sample is plotted (right axis). The following values were set as initial values for the PTP: $\kappa = 1.10$, $\omega_0 = 700$ kHz·mm, and $d\omega = 50$ kHz·mm. The hyperelastic compensating parameters and effective thicknesses are

TABLE VI. RESULTS OF THE PSM PARAMETER FITTING PROCEDURES OF THE FDM AND THE HYPERELASTIC COMPENSATING FUNCTION, $\Phi(\omega)$, FOR THE SILICONE RUBBER SAMPLES SG5x38, SG5x21, AND SG5x11 WITH ESTIMATED UNCERTAINTIES ΔU IN THE 100 TO 250 kHz FREQUENCY RANGE.

Parameter[1]	Fixed value[2]	PTP values[3] SG5x38	SG5x21	SG5x11	Δu[4]
FDM					
k		1.40×10^3	1.36×10^3	1.41×10^3	$\pm 0.01 \times 10^3$
α	0.65[5]				
τ_{c} [ms]		10	10	10	±4
E^{ini} [GPa]		1.00	1.00	1.00	±0.05
E_∞ [GPa]		0.98	0.95	0.99	±0.01
$\Phi(\omega)$					
κ		1.11	1.17	1.16	±0.005
ω_0 [kHz·mm]		764	760	629	±0.5
$d\omega$ [kHz·mm]		104	38.2	5.77	±0.5
h^e [mm]		4.72	4.75	5.15	±0.01
Δu[6]		<0.004	<0.003	<0.007	
ν	0.49				
ρ_e [kg/m^3]	970				

[1]The parameters k, α, and κ are all dimensionless numbers.
[2]Values acquired from external sources (Section II-B-1).
[3]Values determined using the parameter tuning procedure PTP.
[4]The estimated uncertainty has the same dimension as the corresponding parameter.
[5]Value determined from an assumption about α and the static elastic modulus see Section II-B-3.
[6]Error in the fit of $\Phi(\omega)$ after the end of the iteration procedure.
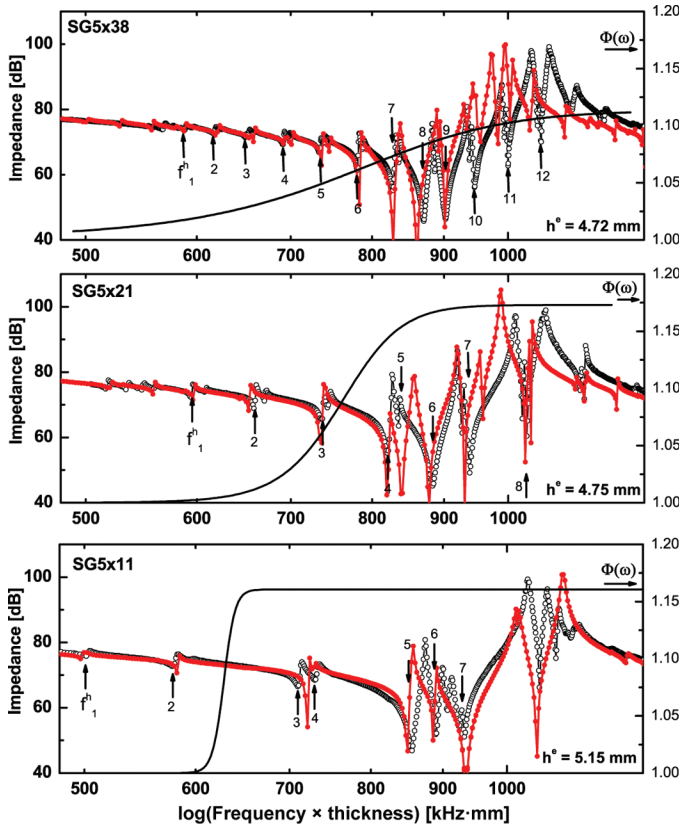
Fig. 11. The PSM calculated and measured electric impedance responses of the PZT-sensor in contact with the silicone rubber disks SG5x38, SG5x21, and SG5x11. (Open circles) measured response; (filled red circles) PSM calculated response. h^e is the effective thickness of the silicone rubber disk. Marked with arrows in each plot is the series of frequency–thicknesses, f_n^h, used to calculate the relative deviation, Δ_n, for each sample. A complete list of all f_n^h in Table VII. For every sample, the hyperelastic compensating function $\Phi(\omega)$ is plotted (right axes).

listed for each sample in Table VI. The calculated and measured frequency–thicknesses, f_n^h, used in the fitting procedures are listed in Table VII for each sample.

B. Results of the Calculated and Measured Impedance Response for Samples SG5x38, SG5x21, and SG5x11

The results are plotted in Fig. 11, where the transitions between the standing Lamb wave modes are shown as peaks superimposed on the first radial resonance of the piezoelectric sensor. The effective thicknesses, h^e, of the samples were 4.70 mm for sample SG5x38, 4.75 mm for sample SG5x21, and 5.15 mm for sample SG5x11. The number of frequencies, n, and the relative deviation, Δ_n, between the calculated and the measured transitions in the impedance response were 12 and 0.7% for sample SG5x38, 8 and 0.6% for sample SG5x21, and 7 and 0.7% for sample SG5x11. The PSM failed to reproduce most of the transitions above the midpoint between the first radial and anti-radial frequency for any of the samples.

V. DISCUSSION

The silicone rubber, SG612, used in this study can be used as a phantom for human soft tissue. As an example, reported values of the skin elastic modulus, measured *in vivo*, are 66 kPa along the axis, and 13 kPa perpendicular to the axis of the arm, measured on humans (63 people) [32].

When emitting vibrations into a silicone rubber phantom with frequencies in the 100 to 250 kHz range, as in the case of the tactile resonance sensor, the elastic modulus of the silicone rubber becomes complex, with a real and imaginary part. According to the determined FDM for the silicone rubber, Fig. 7, the real part of the elastic modulus increases by more than 10^3 times when the rubber is vibrated with a longitudinal wave with a frequency of

TABLE VII. MEASURED AND CALCULATED FREQUENCY–THICKNESSES, f_n^h, (IN kHz·MM) USED IN THE CALCULATION OF THE RELATIVE DEVIATION, Δ_N, FOR THE SILICONE RUBBER SAMPLES.

f_n^h	SG5x38		SG5x21		SG5x11	
	Meas.	Calc.	Meas.	Calc.	Meas.	Calc.
f_1^h	583.1	585.2	594.7	596.1	501.5	497.0
f_2^h	612.5	615.7	659.0	653.1	578.3	579.4
f_3^h	644.4	648.6	731.1	736.3	709.4	718.4
f_4^h	685.6	688.5	820.3	819.4	729.5	726.2
f_5^h	728.1	733.2	835.4	838.4	855.5	849.8
f_6^h	774.4	780.2	883.3	878.8	889.6	885.8
f_7^h	821.3	824.9	938.7	931.0	932.4	934.7
f_8^h	863.8	857.8	1030.7	1028.4		
f_9^h	895.6	900.1				
f_{10}^h	938.8	944.7				
f_{11}^h	991.8	980.0				
f_{12}^h	1047.5	1036.4				
Δ_n		0.007		0.006		0.007

Δ_n = The relative deviation of n Lamb-wave transitions.

100 kHz. The rubber, at that frequency, behaves almost as a glass, with the elastic modulus in the range of gigapascals. The same effect can be achieved if the rubber is cooled to the glass transition temperature, as shown by the time–temperature superposition principle for thermorheologigal simple materials [33]. The loss tangent in the rubber decreases from its maximum value of 1.6 at 3 Hz to 0.003 at 100 kHz. The analysis of the impact of varying the parameter α shows clearly that the real part E' is fairly insensitive, whereas the imaginary part E'' is very sensitive to variations in α within the frequency range of the calculations. This makes the determination of the time constant, τ_c, and α ambiguous because there must exist pairs of τ_c and α that would generate nearly the same result for E' and E'' in the frequency range of the calculations. Because the variation of E'' mainly affects the transition amplitudes in the frequency range of the finite element calculations, one way to determine α would be to fit the FDM to the amplitudes of the Lamb wave transitions for the SG5x38 sample, where we have six transitions within a frequency range of 40 kHz. This approach to determine α relies on optimal contact between the sensor/vibrator and the SRD, because a bad contact would affect the amplitudes of the transitional peaks. A possible way to determine τ_c would be to measure the maximum phase of a longitudinal sinusoidal stress–strain configuration of the silicone rubber, sweeping the frequency to detect the frequency of maximum loss tangent. That would enable α to be separately determined from τ_c. The FDM was validated in the 100 to the 250 kHz frequency range, meaning that when drawing conclusions about the behavior of the complex modulus outside that frequency range, i.e., about the values of the FDM parameters, the values should be regarded as uncertain.

The peaks in the electric impedance frequency response that can be seen in the plots in Fig. 11 are the results of the switching of symmetric standing Lamb wave modes that can take place in the SRD as the frequency increases.

When determining the time-constant, τ_c, in the FDM model, the fitting procedure was based on fitting the amplitudes of the Lamb-mode transitions for the selected mode to the measured amplitudes. The measured amplitudes are strongly correlated to the acoustical coupling between the sensor and the SRD. The cured silicone rubber was very tacky, which improves the acoustic coupling. The amplitudes of the transitions were clearly affected when removing the sensor disk from a cured silicone rubber sample and then putting the sensor back again. Putting ultrasound gel on the contact surface improved the coupling, but it was never restored to the original condition. Fig. 12 shows a graph of the impedance responses of the SG5x38 SRD with the sensor removed and then remounted.

In the Payne effect [30], the complex elastic modulus decreases with increasing periodic strain amplitudes. Payne discovered the effect when loading natural rubber with various proportions of carbon black. The rubber was then exposed to increasing amplitudes of periodic strain.
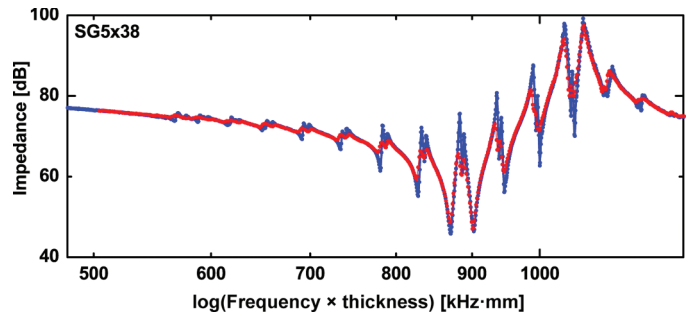

Fig. 12. The effect of removing and the remounting the sensor of the SG5x38 sample. Plot: (filled blue circles) measured impedance response with the sensor in its original position, (solid red circles) measured impedance response with the sensor removed and then remounted with ultrasonic gel on its contact surface.

A prerequisite for the Payne effect is the presence of some type of filler (crystallites or colloids). In the silicone rubber case, colloids of platinum could be the explanation for the effect because a platinum catalyst is used in component B of SG612, and it has been shown that colloids can be formed in platinum catalysts [34].

At the upper end of the frequency–thickness range, the calculated and measured impedance responses do not fit very well, which is true for all three samples. This indicates that the hyperelastic compensating function, $\Phi(\omega)$, is not suitable in the whole frequency range, especially above the mid-point between the minimum and maximum impedance frequencies of the first radial resonance. As seen in Fig. 11, the slope of $\Phi(\omega)$ is correlated to the number of transitions in the impedance frequency response. It seems that the proposed $\Phi(\omega)$ can handle the increase in the transition amplitudes, but not the subsequent decrease in the amplitudes. This also means that $\Phi(\omega)$ lacks generality and can only be applied when the number of transitions and the transition frequencies are known. To be able to compensate for the effect while calculating the response for each frequency step, the constitutive equations of the SRD must be modified to take care of the hyperelastic effect.

VI. Conclusions

The results of the work in this paper show that: 1) the finite element model developed for the thick cylindrical piezoelectric element in contact with the silicone rubber disk is working and produces frequency responses of the electric impedance that can be validated against measured responses with excellent results up to the first radial resonance of the sensor; 2) the complex elastic modulus of silicone rubber is determined, using an inverse method, in the frequency range 100 to 250 kHz, which is the working frequency range of the tactile resonance sensor—the determination of the modulus at other frequencies is approximate; and 3) the method used in this paper utilizing standing Lamb waves clearly has the potential to be a

model system for detecting objects with deviating elastic modulus in a silicone rubber disk. Therefore, our next study will have its focus on this issue.

To our knowledge, the determination of the complex elastic modulus of silicone rubber disks using the method described in this paper is new and has not been done before.

Appendix

The piezoelectric and dielectric permittivity constants are denoted e_{kp} and ε_{ik}, respectively. The elastic stiffness constant, c_{pq}^D, at constant electric flux density, D, can be expressed as

$$
c_{pq}^D = \begin{bmatrix} c_{11}^D & c_{12}^D & c_{13}^D & 0 & 0 & 0 \\ c_{12}^D & c_{11}^D & c_{13}^D & 0 & 0 & 0 \\ c_{13}^D & c_{13}^D & c_{33}^D & 0 & 0 & 0 \\ 0 & 0 & 0 & c_{44}^D & 0 & 0 \\ 0 & 0 & 0 & 0 & c_{44}^D & 0 \\ 0 & 0 & 0 & 0 & 0 & c_{66}^D \end{bmatrix}, \quad c_{66}^D = \frac{(c_{11}^D - c_{12}^D)}{2},
$$

(A1)

where

$$
c_{11}^D = c_{11}^E + \frac{e_{31}^2}{\varepsilon_{33}^S}, \quad c_{12}^D = c_{12}^E + \frac{e_{31}^2}{\varepsilon_{33}^S},
$$

$$
c_{13}^D = c_{13}^E + \frac{e_{31}e_{33}}{\varepsilon_{33}^S}, \quad c_{33}^D = c_{33}^E + \frac{e_{33}^2}{\varepsilon_{33}^S},
$$

$$
c_{44}^D = c_{44}^E + \frac{e_{15}^2}{\varepsilon_{11}^S}.
$$

The matrix h_{kp} is given by

$$
h_{kp} = \begin{bmatrix} 0 & 0 & 0 & 0 & h_{15} & 0 \\ 0 & 0 & 0 & h_{15} & 0 & 0 \\ h_{31} & h_{31} & h_{33} & 0 & 0 & 0 \end{bmatrix},
$$

(A2)

where

$$
h_{15} = \frac{e_{15}}{\varepsilon_{11}^S}, \quad h_{31} = \frac{e_{31}}{\varepsilon_{33}^S}, \quad h_{33} = \frac{e_{33}}{\varepsilon_{33}^S}.
$$

The inverted dielectric permittivity constant, β_{ik}^S, at constant strain S is

$$
\beta_{ik}^S = \begin{bmatrix} \beta_{11}^S & 0 & 0 \\ 0 & \beta_{11}^S & 0 \\ 0 & 0 & \beta_{33}^S \end{bmatrix},
$$

(A3)

where

$$
\beta_{11}^S = \frac{1}{\varepsilon_{11}^S}, \quad \beta_{33}^S = \frac{1}{\varepsilon_{33}^S}.
$$

References

[1] P. N. T. Wells, "Ultrasonic imaging of the human body," *Rep. Prog. Phys.*, vol. 62, no. 5, pp. 671–722, 1999.

[2] D. Gyrd-Hansen, "Is it cost effective to introduce screening programmes for colorectal cancer?" *Health Policy*, vol. 41, no. 5, pp. 189–199, 1997.

[3] Y. Wang, M. Raj, H. S. McGuff, G. Bhave, B. Yang, T. Shen, and X. Zhang, "Portable oral cancer detection using a miniature confocal imaging probe with a large field of view," *J. Micromech. Microeng.*, vol. 22, no. 6, art. no. 065001, 2012.

[4] V. Jalkanen, B. M. Andersson, A. Bergh, B. Ljungberg, and O. A. Lindahl, "Resonance sensor measurements of stiffness variations in prostate tissue in vitro—A weighted tissue proportion model," *Physiol. Meas.*, vol. 27, no. 12, pp. 1373–1386, 2006.

[5] S. Candefjord, K. Ramser, and O. A. Lindahl, "Technologies for localization and diagnosis of prostate cancer," *J. Med. Eng. Technol.*, vol. 33, no. 8, pp. 585–603, 2009.

[6] M. O. Culjat, D. Goldenberg, P. Tewari, and R. S. Singh, "A review of tissue substitutes for ultrasound imaging," *Ultrasound Med. Biol.*, vol. 36, no. 6, pp. 861–873, 2010.

[7] T. J. Hall, M. Bilgen, M. F. Insana, and T. A. Krouskop, "Phantom materials for elastography," *IEEE Trans. Ultrason. Ferroelectr. Freq. Control*, vol. 44, no. 6, pp. 1355–1365, 1997.

[8] A. Eklund, A. Bergh, and O. A. Lindahl, "A catheter tactile sensor for measuring hardness of soft tissue: Measurement in a silicone model and in an *in vitro* human prostate model," *Med. Biol. Eng. Comput.*, vol. 37, no. 5, pp. 618–624, 1999.

[9] V. Jalkanen, B. M. Andersson, A. Bergh, B. Ljungberg, and O. A. Lindahl, "Prostate tissue stiffness as measured with a resonance sensor system: A study on silicone and human prostate tissue *in vitro*," *Med. Biol. Eng. Comput.*, vol. 44, no. 7, pp. 593–603, 2006.

[10] A. P. Astrand, V. Jalkanen, B. M. Andersson, and O. A. Lindahl, "Contact angle and indentation velocity dependency for a resonance sensor—Evaluation on soft tissue silicone models," *J. Med. Eng. Technol.*, vol. 37, no. 3, pp. 185–196, 2013.

[11] M. Y. Jansen, "A viscoelastic skin model," Master's thesis, Computational and Experimental Mathematics, Eindhoven University of Technology, Eindhoven, The Netherlands, 1996.

[12] A. Passot and G. Cabodevila, "Mechanical properties of an artificial vascularized human skin," in *Proc. SPIE*, vol. 8068, 2011, art. no. 80680C.

[13] M. Kauer, V. Vuskovic, J. Dual, G. Szekely, and M. Bajka, "Inverse finite element characterization of soft tissues," *Med. Image Anal.*, vol. 6, no. 3, pp. 275–287, 2002.

[14] U. G. Jonsson, B. M. Andersson, and O. A. Lindahl, "A FEM-based method using harmonic overtones to determine the effective elastic, dielectric, and piezoelectric parameters of freely vibrating thick piezoelectric disks," *IEEE Trans. Ultrason. Ferroelectr. Freq. Control*, vol. 60, no. 1, pp. 243–255, 2013.

[15] A. Ali, M. Hosseini, and B. B. Sahari, "A review of constitutive models for rubber-like materials," *Am. J. Eng. Appl. Sci.*, vol. 3, no. 1, pp. 232–239, 2010.

[16] K. J. Parker, D. Fu, S. M. Graceswki, F. Yeung, and S. F. Levinson, "Vibration sonoelastography and detectability of lesions," *Ultrasound Med. Biol.*, vol. 24, no. 9, pp. 1437–1447, 1998.

[17] H. Eskandari, S. E. Salcudean, R. Rohling, and J. Ohayon, "Viscoelastic characterization of soft tissue from dynamic finite element models," *Phys. Med. Biol.*, vol. 53, no. 22, pp. 6569–6590, 2008.

[18] R. L. Bagley and P. J. Toevik, "A theoretical basis for the application of fractional calculus to viscoelasticity," *J. Rheol.*, vol. 27, no. 3, pp. 201–210, 1983.

[19] Y. C. Lu, "Fractional derivative viscoelastic model for frequency-dependent complex moduli of automotive elastomers," *Int. J. Mech. Mater. Des.*, vol. 3, no. 4, pp. 329–336, 2006.

[20] K. F. Graff, *Wave Motion in Elastic Solids.* Oxford, UK: Clarendon, 1975.

[21] I. Z. Nenadic, M. W. Urban, S. A. Mitchell, and J. F. Greenleaf, "Lamb wave dispersion ultrasound vibrometry (LDUV) method for quantifying mechanical properties of viscoelastic solids," *Phys. Med. Biol.*, vol. 56, no. 7, pp. 2245–2264, 2011.

[22] B. A. Auld, *Acoustic Fields and Waves in Solids I.* New York, NY: Wiley, 1973.

[23] *IEEE Standard on Piezoelectricity*, ANSI/IEEE Std. 176–1987, 1988.

[24] T. Ikeda, *Fundamentals of Piezoelectricity.* New York, NY: Oxford University Press, 1990.

[25] P. Lunde and M. Vestrheim, "Modelling of loss effects in piezoelectric materials, and adaptation to measurements on radial and thickness modes in thin disks," in *Proc. 15th Int, Congress on Acoustics*, 1995, vol. 1, pp. 381–384.

[26] J. Fehrenbach, "Influence of Poisson's ratio on elastographic direct and inverse problems," *Phys. Med. Biol.*, vol. 52, no. 3, pp. 707–716, 2007.

[27] B. A. Auld, *Acoustic Fields and Waves in Solids II.* Malabar, FL: Krieger, 1990.

[28] F. Dinzart and P. Lipinski, "Improved five-parameter fractional derivative model for elastomers," *Arch. Mech.*, vol. 61, no. 6, pp. 459–474, 2009.

[29] A. W. Mix and A. J. Giacomin, "Standardized polymer durometry," *J. Test. Eval.*, vol. 39, no. 4, pp. 696–705, 2011.

[30] A. R. Payne, "The dynamic properties of carbon black-loaded natural rubber vulcanizates," *J. Appl. Polym. Sci.*, vol. 6, no. 19, pp. 57–63, 1962.

[31] M. M. Oumarou, D. Jeulin, J. Renard, and P. Castaing, "Multi-scale statistical approach of the elastic and thermal behavior of a thermoplastic polyamid-glass fiber composite," *Tech. Mech.*, vol. 32, pp. 484–506, 2012.

[32] F. Khatyr, C. Imberdis, P. Vescovo, D. Varchon, and J.-M. Legarde, "Model of the viscoelastic behaviour of skin in vivo and study of anisotrophy," *Skin Res. Technol.*, vol. 10, no. 2, pp. 96–103, 2004.

[33] G. D. Airey, J. Wilmot, R. A. Grenfell, D. J. Irvine, I. A. Barker, and J. E. Harfi, "Rheology of polycarbonate binders produced via catalytic chain transfer polymerization as an alternative to bitumen in road pavement materials," *Eur. Polym. J.*, vol. 47, no. 6, pp. 1300–1314, 2011.

[34] L. N. Lewis, J. Stein, Y. Gao, and R. E. Colborn, "Platinum catalysts used in the silicones industry," *Platin. Met. Rev.*, vol. 41, no. 2, pp. 66–75, 1997.

Olof A. Lindahl was born in Örnsköldsvik, Sweden, in 1955. He received his Ph.D. in biomedical engineering in 1993. He became associate professor 1996 and professor 1999 in biomedical engineering at Umeå University, Sweden. He is currently a professor in biomedical engineering at Umeå University and at Luleå University of Technology, Sweden. His main position is as head of the biomedical R&D department at the University Hospital of Northern Sweden. He is an inventor of 7 granted patents and is also a founder and co-founder of several research spin-off companies and an interdisciplinary biomedical engineering research center, CMTF, where he is director. Professor Lindahl was awarded the Erna Ebeling prize in 2008 for his scientific research and for leadership in the area of science and business in biomedical engineering. He is a member of the International Federation for Medical and Biological Engineering Administrative Council and its General Assembly, and a member of the scientific advisory board of the Swedish Society for Biomedical Engineering and Physics. His research interest is focused on biomedical sensors for detection of prostate cancer, specifically resonance and optical sensors. He has produced more than 100 scientific publications and book chapters in the area of biomedical engineering and business development.

Britt M. Andersson was born in Umeå, Sweden, in 1962. She received her B.Sc. degree in physics in 1988 and her Ph.D. degree in experimental physics in 1993, both from Umeå University, Sweden. She is currently an associate professor in the Department of Applied Physics and Engineering at Umeå University, with research interests in material physics, electroceramics, sensors, and biomedical engineering.

Ulf G. Jonsson received his B.Sc. degree in mathematics and physics in 1973, his Ph.Lic. degree in experimental physics in 1999, and his Ph.D. degree in applied electronics with specialization in biomedical engineering in 2014, all from Umeå University, Sweden (UmU). From 1977 to 1981 and from 1984 to 1993, he worked as a university lecturer in the Department of Physics, UmU. He served at the Swedish institute of defense, FOA 4 Umeå, as researcher from 1981 to 1983. From 1994 to 2009, he worked as a university lecturer in the Department of Applied Physics and Engineering at UmU. In 2001, he and two colleagues received the pedagogical prize of the faculty of Science and Technology for introducing new technologies combined with student-focused methods. Currently, he is working at the biomedical engineering research center, CMTF, Umeå University. His research area is analyzing piezoelectric sensors and soft tissue properties using finite element methods.